

Boundary-Aware 3D Object Detection from Point Clouds

Rui Qian
Renmin University of China
Beijing, China
rui-qian@ruc.edu.cn

Xin Lai
Renmin University of China
Beijing, China
laixin@ruc.edu.cn

Xirong Li*
Renmin University of China
Beijing, China
xirong@ruc.edu.cn

ABSTRACT

Currently, existing state-of-the-art 3D object detectors are in two-stage paradigm. These methods typically comprise two steps: 1) Utilize region proposal network to propose a fraction of high-quality proposals in a bottom-up fashion. 2) Resize and pool the semantic features from the proposed regions to summarize ROI-wise representations for further refinement. Note that these ROI-wise representations in step 2) are considered individually as an uncorrelated entry when fed to following detection headers. Nevertheless, we observe these proposals generated by step 1) offset from ground truth somehow, emerging in local neighborhood densely with an underlying probability. Challenges arise in the case where a proposal largely forsakes its boundary information due to coordinate offset while existing networks lack corresponding information compensation mechanism. In this paper, we propose BANet for 3D object detection from point clouds. Specifically, instead of refining each proposal independently as previous works do, we represent each proposal as a node for graph construction within a given cut-off threshold, associating proposals in the form of local neighborhood graph, with boundary correlations of an object being explicitly exploited. Besides, we devise a lightweight *Region Feature Aggregation Network* to fully exploit voxel-wise, pixel-wise, and point-wise feature with expanding receptive fields for more informative ROI-wise representations. As of Apr. 17th, 2021, our BANet achieves on par performance on KITTI 3D detection leaderboard and ranks 1st on *Moderate* difficulty of *Car* category on KITTI BEV detection leaderboard. The source code will be released once the paper is accepted.

CCS CONCEPTS

- Computing methodologies → 3D Object detection; Scene understanding for robotics; Graph neural networks.

KEYWORDS

3D object detection, autonomous driving, graph neural network, boundary aware, point clouds

1 INTRODUCTION

Scene understanding has been a long-term joint interest of multimedia [27] and computer vision [47]. 3D object detection is to estimate 3D bounding boxes from sensory data for objects in the real world, out of which point clouds are increasingly prevalent in the context of autonomous driving, with informative geometric attributes being facilitated. Despite existing efforts [1, 8, 28], it has still trailed 2D object detection thus far [7, 11, 12, 14, 20, 21, 29–31, 47].

*Xirong Li is the Corresponding author(E-mail: xirong@ruc.edu.cn).

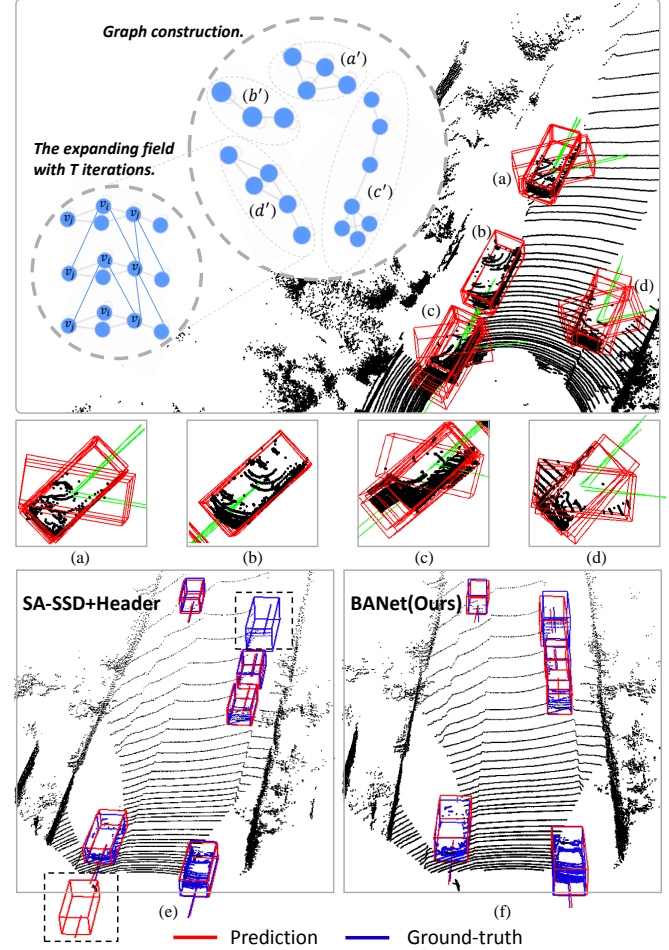


Figure 1: Representative proposals (red) predicted by BANet in stage one, leveraging SA-SSD [10] as backbone. Proposals in (a), (c), (d) deviate somehow in cases where azimuth or coordinate offsets from ground truth. In fact, proposals in (b) are exactly what we anticipate in the stage two. (e), (f) illustrate 3D detection results predicted by SA-SSD+detect header and our method (BANet), respectively. The missed and false detection are highlighted with black dotted box.

Existing state-of-the-art point clouds based 3D detectors can be grouped into three genres in the perspective view of representation learning, i.e., voxel-based, point-based, and point-voxel-based methods. Voxel-based methods [17, 34, 39, 42, 46] generally rasterize irregular point clouds into volumetric grids to extract features

from regular domains. Point-based methods [33, 35, 40] simply consume raw point clouds to abstract features from irregular domains. Very recently, a large body of investigations have been looking into fusing the best of two worlds together for synergies. Point-voxel-based methods [3, 10, 32, 41] are considered as a joint treatment to learn more informative representations from both regular and irregular domains.

Note that recent high-performance 3D detectors are similar [32–34, 41]. These methods typically comprise two steps: 1) Utilize region proposal network to propose a fraction of high-quality proposals in a bottom-up fashion. Usually, these proposals scatter in local neighborhood densely with an underlying probability, as shown in Figure 1 in red. 2) Resize and pool the semantic features from the proposed regions to summarize ROI-wise representations for further refinement. Note that these ROI-wise representations in step 2) are considered individually as an uncorrelated entry when fed to following detection headers. As illustrated in Figure 1, proposals in (a), (c), (d) deviate somehow in cases where azimuth or coordinate offsets from ground truth while proposals in (b) are exactly what we anticipate. Particularly, coordinate offset is even salient at long ranges due to the high sparseness of point clouds by nature. **Challenges arise in the case where a proposal largely forsakes its boundary information due to coordinate offset while existing networks lack corresponding information compensation mechanism.** As a result, considerable proposals generated by step 1) could not perceive a complete boundary of an object individually. On the basis of above discussion and analysis, a new challenge arises: can we associate these selected proposals in local neighborhood together so that each proposal could achieve the whole receptive field of an object?

Bearing this in mind, we propose Boundary-Aware Graph Neural Network (*BANet*) for 3D object detection from point clouds. As shown in Figure 1, (a'), (b'), (c'), and (d') are the corresponding graph representations of the proposals in neighborhood, (a), (b), (c), (d). Instead of refining each proposal independently as previous works do [32–34, 41], we represent each proposal as a node for graph construction within a distance threshold, modeling local boundary correlations of an object in the form of local neighborhood graph. Messages flow freely between nodes through spurious edges iteratively. As a result, each proposal is expected to achieve a complete boundary of the object with an expanding receptive field through multiple iterations.

To fully exploit informative semantic features extracted from corresponding regions, we propose a lightweight *Region Feature Aggregation Network* (AggNet). Specifically, to compensate for the absence of 3D structure context when directly converting 3D feature map into BEV representation, we devise a Voxel-Point Hybrid module to restore voxel-wise features from 3D backbone network; to eliminate extensive computation overheads when filtering dense proposals as traditional ROI pooling operation does, we adapt a simplified variant from SA-SSD [10] for pixel-wise feature extraction; to densify gradually downsampled 3D feature volumes, we train a PointNet(++) [25] network from scratch to inject original geometric structure from point-wise features. Our final ROI-wise representations for each node on the local neighborhood graph is obtained by aggregating associated voxel-wise, pixel-wise, and

point-wise features together, before fed through boundary-aware graph neural network for further refinement.

Below, we summarize our contributions into three facets. 1) We propose BANet framework which effectively models local boundary correlations of an object in the form of local neighborhood graph, which explicitly facilitates a complete boundary for each individual proposal by the means of an information compensation mechanism. 2) We propose a lightweight region feature aggregation network to make use of informative semantic features, leading to significant improvement with manageable memory overheads. 3) Our BANet outperforms all previous state-of-the-art methods with remarkable margins on KITTI BEV detection leaderboard and ranks 1st on *Car* category of *Moderate* difficulty as of Apr. 17th, 2021. Furthermore, comprehensive experiments are conducted on KITTI Dataset in diverse evaluation settings to analyze the effectiveness of BANet.

2 RELATED WORK

Representation learning in regular domains. Voxel-based methods [17, 39, 42, 46] generally voxelize raw point clouds into compact volumetric grids, resorting to 3D sparse convolution neural network for representation learning. These methods are amenable to hardware implementations while suffer from information loss due to quantization error. Limited voxel resolution inevitably hinders more fine-grained localization accuracy. The seminal work VoxelNet [46] takes the first lead to rasterize a point cloud into more compact 3D voxel representations and leverages a lightweight PointNet-like [24, 25] block to transform points within each voxel into a voxel-wise representation, followed by 3D CNNs for spatial context aggregation and detections generation. SECOND [39] utilizes 3D sparse convolution as a substitute of conventional 3D convolution to only convolve against non-empty voxels. PointPillars [17] partitions points into “pillars” rather than voxels to get rid of the need of convolving against 3D space via forming an 2D pseudo BEV image straight forward.

Representation learning in irregular domains. Point-based methods usually takes raw point clouds as inputs. Powered by PointNet [24, 25] or Graph Neural Network [9, 15, 26, 37, 38], these methods at utmost preserve 3D structure context from real 3D world with flexible receptive fields. Nevertheless, they are hostile to memory overheads and sensitive to translation variance. These methods are typically exemplified by PointRCNN [33], which leverages PointNet(++) [25] to segment foreground points from raw point clouds for the purpose of reducing 3D search space, elegantly inheriting the ideology of Faster RCNN [31] architecture. 3DSSD [40] safely removes the core feature propagation layer of PointNet(++) [25] by introducing F-FPS to compensate for the loss of foreground points when downsampling. Point-GNN [35] seeks to generalize graph neural networks (GNNs) to 3D object detection via constructing a graph over downsampled raw point clouds. Few investigations have successfully transplanted GNNs for object detection til Shi et al. proposed Point-GNN. Our BANet differs from Point-GNN by constructing local neighborhood graphs over ROI-wise high semantic features rather than raw point clouds.

Representation learning in hybrid domains. Very recently, a fusion strategy to bring the best of two worlds together is increasingly prevalent. Point-voxel-based methods [3, 10, 32, 41] deeply

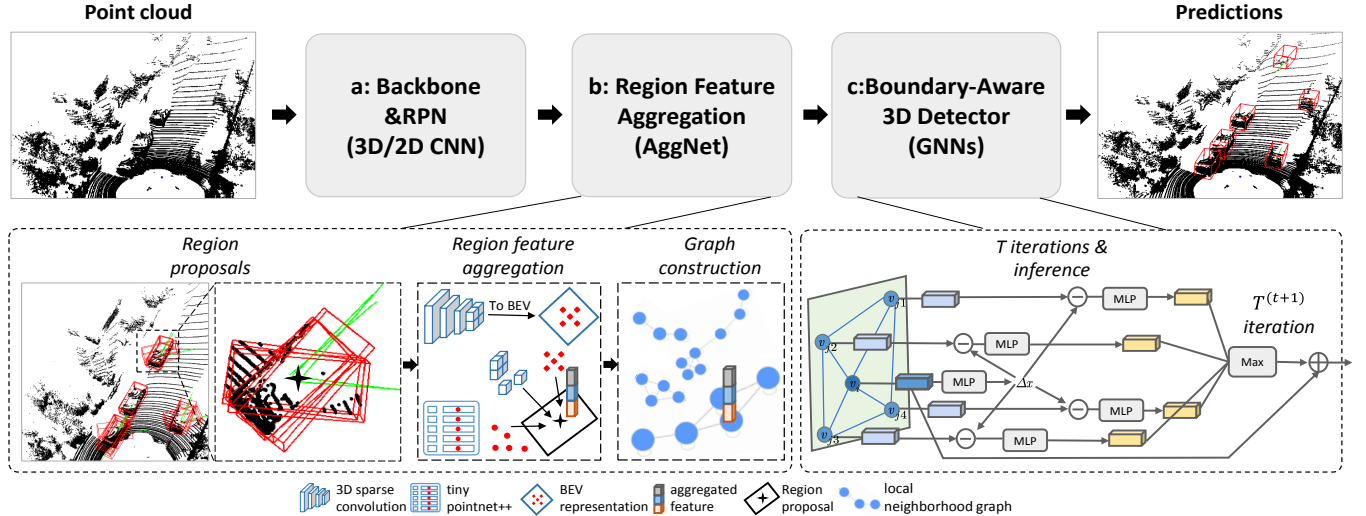


Figure 2: Overview of our proposed BANet. BANet includes three key components: (a) Backbone and Region Proposal Network. We first voxelize the raw point clouds into volumetric grids, resorting to backbone network with a series of 3D sparse convolutions for multi-scale semantic feature abstraction and 3D proposal generation. (b) Region Feature Aggregation Network, which fully exploits multi-level semantic features for more informative RoI-wise representations. (c) Boundary-Aware Graph Neural Network, which takes 3D proposals in immediate neighborhood as inputs for graph construction within a given cut-off distance, associating uncorrelated proposals in the form of local neighborhood graph, with boundary correlations of an object being explicitly informed through an information compensation mechanism.

integrate 3D sparse convolution operation from voxel-based methods and the flexible receptive fields from point-based methods. PVConv [22] demonstrates the effectiveness of the combinations of coarse-grained voxel-wise features and fine-grained point-wise features for synergies. STD [41] voxelizes point-wise features for 3D region proposals and exploits more generic spherical anchors rather than rectangular ones to achieve a high recall and alleviates computational overheads. PV-RCNN [32] leverages set abstraction operation among voxels instead of raw point clouds to achieve flexible receptive fields for fine-grained patterns while maintains computational efficiency. SA-SSD [10] introduces an auxiliary network to consolidate the correlations of 3D feature volumes under the supervision of point-level geometric properties.

3 PROPOSED BANET

In this section, we propose BANet, which effectively models local boundary correlations of an object by the means of local neighborhood graphs, explicitly facilitating a complete boundary for each individual proposal with an information compensation mechanism. As illustrated in Figure 2, our BANet includes: (a) backbone and region proposal network, (b) a region feature aggregation network and (c) a boundary-aware graph neural network. Specifically, we first leverage 3D sparse convolutions for semantic feature extraction from voxelized raw point clouds, and then reshape the output of 3D backbone to BEV representation, on which a region proposal network is employed for high-quality 3D proposal generation. Subsequently, we construct boundary-aware graphs over these proposals in local neighborhood for further refinement. Although BEV representation is informative (see Sec. 4.3.1), such an underlying

mechanism suffers from two drawbacks: 1) BEV representation stems from gradually downsampled 3D feature volumes from the output of 3D backbone, which inevitably dilutes its features. 2) BEV representation forsakes 3D structure context without ever recovering from the squeezed depth dimensions. As such, we devise a lightweight region feature aggregation network to alleviate the information loss via aggregating voxel-wise, pixel-wise, and point-wise feature closely for more informative RoI-wise representations.

This section is organized as follows. Sec. 3.1 describes our backbone and region proposal network. Sec. 3.2 introduces the proposed boundary-aware graph neural network. Sec. 3.3 introduces region feature aggregation network. Sec. 3.4 presents training objectives.

3.1 Backbone and Region Proposal Network

3.1.1 Voxelization. We first follow a many-to-one mapping algorithm [10, 39, 46] to voxelize the raw point clouds for representation learning. Specifically, let p be a point in a raw point cloud \mathcal{P} with 3D coordinates (p_x, p_y, p_z) and reflectance intensities p_r , where $\mathcal{P} = \{p^i = (p_x^i, p_y^i, p_z^i, p_r^i) \in \mathbb{R}^4 : i = 1, \dots, N\}$, N indicates the number of points within a point cloud. Denote by $\{\left(\lfloor \frac{p_x^i}{v_L} \rfloor, \lfloor \frac{p_y^i}{v_W} \rfloor, \lfloor \frac{p_z^i}{v_H} \rfloor\right) : i = 1, \dots, N\}$ the voxel index of each point p^i in \mathcal{P} , where $\lfloor \cdot \rfloor$ indicates floor function. $[v_L, v_W, v_H] \in \mathbb{R}^3$ is the spatial volume of a voxel v , where $v = \{p^i = (p_x^i, p_y^i, p_z^i, p_r^i)\}^T \in \mathbb{R}^4 : i = 1, \dots, t\}$ represents a non-empty voxel, comprising t points with the same voxel index under voxel occupancy of \mathcal{T} ($t \leq \mathcal{T}$). A point cloud \mathcal{P} can be evenly devided into a feature map with a resolution of $L \times W \times H$ according the voxel volume of $[v_L, v_W, v_H]$. We iteratively identify

which voxel each point p^i belongs to based on the associated index. For simplicity, we calculate centroid within each voxel for the initial voxel representation $f(v) = \left\{ \frac{1}{t} \sum_{i=1}^t (p_x^i, p_y^i, p_z^i, p_r^i) : i = 1, \dots, M \right\}$, M indicates the number of voxels in a point cloud.

3.1.2 Network architecture. As shown in Figure 2, we follow the architecture in [17, 32, 39, 46] to employ 3D backbone and 2D backbone network to summarize features for BANet. 3D backbone network [17, 32, 39, 46] downsamples 3D feature volumes $8 \times$ from point clouds with a series of $3 \times 3 \times 3$ sub-manifold sparse convolutions, each of which follows a batch normalization and non-linear ReLU function. 2D backbone network simply stacks six standard convolutions with kernel size of 3×3 , to convolve against 2D bird-view feature maps reshaped from the output of 3D backbone network for further feature abstraction. Our detection header comprises two sibling 1×1 standard convolutions, generating high-quality 3D proposals in a pixel-by-pixel fashion for the following graph construction (see Sec. 4.1.2).

3.2 Boundary-Aware Graph Neural Network

In this section, we describe our boundary-aware graph neural network. We assume that we have already obtained 3D proposals and their corresponding RoI-wise representations. We first describe how the graph is constructed (see Sec. 3.2.1). We then detail graph update algorithm (see Sec. 3.2.2).

3.2.1 Graph construction. Consider an F -dimensional detection set with n 3D proposals, denoted by $X = \{x_1, \dots, x_n\} \subseteq \mathbb{R}^F$, where $x_i = (x_i, s_i)$ is regarded as a node of graph \mathcal{G} with 3D coordinates $x_i \in \mathbb{R}^3$ and initial node state $s_i \in \mathbb{R}^F$ of a 3D proposal. In our case, we construct local neighborhood graph $\mathcal{G}(\mathcal{V}, \mathcal{E})$ of X in \mathbb{R}^F as

$$\mathcal{E} = \{(i, j) \mid \|x_i - x_j\|_2 < r\}, \quad (1)$$

where $\mathcal{V} = \{1, \dots, n\}$ and $\mathcal{E} \subseteq \mathcal{V} \times \mathcal{V}$ are the nodes and edges, respectively, r is the given cut-off threshold. $\mathcal{G}(\mathcal{V}, \mathcal{E})$ is undirected, which includes self-loop, meaning each node connecting to itself. In this work, we define $\mathcal{N}(i)$ as neighborhood function, which draws neighbors from the set $\{j \in \mathcal{V} : (i, j) \in \mathcal{E}\}$ with a runtime complexity $O(c|\mathcal{V}|)$ in the worst case, where c is an user-specified constant.

3.2.2 Graph update. The main idea described in Algorithm 1 is that each node of $\mathcal{G}(\mathcal{V}, \mathcal{E})$ updates itself via aggregating information from their immediate neighbors at the previous iteration. As information flows over nodes, each node gradually gains an expanding receptive field from further reaches of its neighbors. As described in Algorithm 1, k in the outer loop represents the current step, h_k indicates the hidden state of a node at present step. In the vanilla version, $\{h_j^{k-1}, \forall j \in \mathcal{N}(i)\}$ denotes associated feature vectors of the local neighbors of node $i \in \mathcal{V}$, which is directly concatenated before fed through a multi-layer perceptron network (MLP) for feature transformation. We then aggregate these transformed features into a single vector, $h_{\mathcal{N}(i)}^k$, via aggregation operator. In this paper, we adopt $\max(\cdot)$ aggregator inspired by recent advances in leveraging graph neural network to learn feature representations over point sets [35].

Algorithm 1: The vanilla graph update algorithm

Input: Graph $\mathcal{G}(\mathcal{V}, \mathcal{E})$; input features $\{x_i, \forall i \in \mathcal{V}\}$; depth K ; weight matrices $\mathbf{W}_g^k, \mathbf{W}_f^k, \forall k \in \{1, \dots, K\}$; non-linearity σ ; channel-wise symmetric aggregator function \square_k (e.g., Σ or \max), $\forall k \in \{1, \dots, K\}$; concatenation function: CAT along aixs 1 dimension; neighborhood function $\mathcal{N} : i \rightarrow 2^{\mathcal{V}}$.

Output: Vector representations z_i for all $i \in \mathcal{V}$.

```

1  $h_i^0 \leftarrow x_i, \forall i \in \mathcal{V}$ ;
2 for  $k = 1 \dots K$  do
3   for  $i \in \mathcal{V}$  do
4      $h_{\mathcal{N}(i)}^k \leftarrow \square_k \left( \mathbf{W}_g^k \cdot CAT \left( \{h_j^{k-1}, \forall j \in \mathcal{N}(i)\} \right) \right)$ ;
5      $h_i^k \leftarrow h_i^{k-1} + \sigma \left( \mathbf{W}_f^k \cdot h_{\mathcal{N}(i)}^k \right)$ ;
6   end
7 end
8  $z_i \leftarrow h_i^K, \forall i \in \mathcal{V}$ .

```

To alleviate translation variance mentioned in [35, 40], we extend our graph propagation strategy via concatenating the relative coordinates $x_i - x_j$ to the semantic feature of the node $j \in \mathcal{V}$ within the neighborhood of center node $i \in \mathcal{V}$. Furthermore, given x_i already contains local structure context from previous iteration, we follow [35] to predict an alignment offset Δx_i^k for each node in $\mathcal{N}(i)$. Let $[\cdot]$ be an element-wise concatenation and thus the final aggregated feature in this paper is obtained by:

$$h_{\mathcal{N}(i)}^k \leftarrow \max_k \left(\mathbf{W}_g^k \cdot CAT \left(\left[\left[x_i - x_j + \Delta x_i^k, h_j^{k-1} \right], \forall j \in \mathcal{N}(i) \right] \right) \right). \quad (2)$$

3.2.3 Graph header. We introduce two sibling branches, which takes z_i as inputs with two stacked MLP layers for refinement: one is for bounding box classification, and the other is for more accurate oriented 3D bounding box regression.

3.3 Region Feature Aggregation Network

The art of feature aggregation for RoI-wise representation is of significance (see Sec. 4.3.1). As aforementioned, BEV representation is informative. Nevertheless, such an underlying mechanism induces information loss, which degrades more accurate localization. In contrast, by aggregating voxel-wise, pixel-wise, and point-wise feature together, we achieve the top performance. In a sequel, we specify the details of each feature component.

3.3.1 Voxel-wise feature encoding. To obtain voxel-wise feature, we devise a lightweight Voxel-Point Hybrid module to fully exploit the merits of both voxel-based and point-based methods [22, 32]. Specifically, we restore the real-world 3D coordinate for each voxel from nonzero index on the basis of a quantization step at current stage, together with its corresponding 3D sparse convolution features, that is, each voxel is in the form of $\{(f_j, p_j) : j = 1, \dots, M\}$, where f_j denotes 3D sparse convolution feature and p_j indicates the real-world coordinate of a voxel centroid. To associate multi-scale features at different stage, we broadcast these 3D sparse convolution features into raw point clouds via feature propagation algorithm

mentioned in [25]. We then interpolate 3D sparse convolution features $\mathbf{f}^{(voxel)}$ from raw point clouds, which compensates for the information loss of directly converting 3D sparse convolution feature map into 2D BEV representation without ever restoring its 3D structure context.

3.3.2 Pixel-wise feature encoding. To obtain our pixel-wise feature from BEV representation, we employ a variant of RoI pooling operation adapted from SA-SSD [10]. Specifically, for each 3D proposal, we generate $m \times n$ evenly spaced mesh grids along x - and y -axis in the BEV perspective of a 3D proposal, respectively. We then encode BEV representation into $m \times n$ feature maps. For each mesh grid point, we interpolate one position over a single feature map via spatial transformer sampler [13] to form the final pixel-wise feature component $\mathbf{f}^{(pixel)} \in \mathbb{R}^{m \times n}$ of RoI-wise representation at negligible cost. Pixel-wise feature can be extracted by any traditional RoI pooling operation in practice. Whereas, traditional pooling mechanism suffers from expensive computation overheads.

3.3.3 Point-wise feature encoding. To compensate for the information loss induced by quantization error [32, 40], we employ an adapted PointNet(++) [25] variant. Specifically, we leverage the commonly used backbone [17, 39, 46] to gradually $8 \times$ downsample 3D feature maps for the purpose of memory usage saving, which dilutes 3D features inevitably. We train a tiny PointNet from scratch, which consumes raw point clouds as inputs to summarize the whole scene into a fraction of keypoints' semantic features, which are broadcast into the centroids of the proposed 3D proposals to obtain point-wise feature component, $\mathbf{f}^{(point)}$, with the help of feature propagation algorithm in [25].

Finally, we summarize the three aforementioned multi-level associated feature components via concatenation to enrich the final RoI-wise representations for graph construction in the stage two, which significantly contributes to the performance (see Sec. 4.3.2),

$$\mathbf{X} = \left\{ \mathbf{x}_i = \left(\mathbf{x}_i, \left[\mathbf{f}_i^{(voxel)}, \mathbf{f}_i^{(pixel)}, \mathbf{f}_i^{(point)} \right] \right) : i = 1, \dots, n \right\}. \quad (3)$$

3.4 Loss Functions

To learn informative representations in a fully unsupervised fashion, we follow the conventional anchor-based settings in [39]. In particular, we use Focal Loss [20], Smooth-L1 Loss for the bounding box classification and regression, respectively in both stage one (\mathcal{L}_{rpn}) and stage two (\mathcal{L}_{gnn}). To obtain better boundary-aware voxel-wise representations, we introduce a center offset estimation branch:

$$\mathcal{L}_{offset} = \frac{1}{N_{pos}} \sum_i^N \mathcal{L}_{smooth-L1} \left(\Delta \hat{d} - \Delta d^* \right) \cdot \mathbb{1} [b_i^* \geq 1], \quad (4)$$

where Δd^* indicates the offsets of interior points of a ground-truth bounding box from center coordinate, N_{pos} represents the number of foreground points, $\mathbb{1} [b_i^* \geq 1]$ indicates only the points fall in ground-truth bounding box are considered. Besides, we also consider foreground segmentation as

$$\mathcal{L}_{seg} = \frac{1}{N_{pos}} \sum_i^N -\alpha (1 - \hat{p}_i)^\gamma \log (\hat{p}_i), \quad (5)$$

where \hat{p}_i indicates the predicted foreground probability. The overall loss \mathcal{L} is formulated as

$$\mathcal{L} = \mathcal{L}_{rpn} + \mathcal{L}_{gnn} + \mathcal{L}_{offset} + \mathcal{L}_{seg}. \quad (6)$$

4 EVALUATION

In this section, we introduce experimental setup of BANet, including dataset, network architecture, as well as training and inference details (Sec. 4.1). We evaluate on the KITTI Dataset [5, 6] and report comparisons with previous state-of-the-art methods (Sec. 4.2). In Sec. 4.3, extensive ablation studies are conducted on KITTI Dataset in diverse evaluation settings to investigate the effectiveness of each component of BANet. Also, we report runtime analysis for future optimization (Sec. 4.4).

4.1 Experimental Setup

4.1.1 Dataset. The *KITTI Dataset* [5, 6] consists of 7,481 training samples and 7,518 testing samples of three categories (i.e., *Car*, *Pedestrian*, and *Cyclist*) in the context of autonomous driving, each of which has three difficulty levels (i.e., *Easy*, *Moderate*, and *Hard*) according to object scale, occlusion, and truncation levels. As a common practice mentioned in [2], we evaluate our proposed BANet on the KITTI 3D/BEV object detection benchmark following the frequently used *train/val* split to further divide the training samples into a *training* set (3,712 samples) and a *validation* set (3,769 samples) with no overlap. Following previous literature [10, 39], we report the performance on the most commonly-used car category for comparison. To evaluate the performance of BANet on *val* set, we utilize the *train* split for training. To fairly evaluate the proposed BANet's performance on *test* set, of which the labels are unavailable, we train on all *train+val* data and use the parameters of last epoch for online test server submission.

4.1.2 Network Architecture. As shown in Figure 4, we follow the architecture in [17, 32, 39, 46] to design 3D backbone and 2D backbone network for BANet. 3D backbone network [17, 32, 39, 46] downsamples 3D feature volumes from point clouds with dimensions 16, 32, 64, 64, respectively, each of which comprises a series of $3 \times 3 \times 3$ sub-manifold sparse convolutions, together with a batch normalization and nonlinear ReLU following each convolution. 2D backbone network stacks six standard convolutions with filter number of 256, of which kernel size is 3×3 , to convolve against 2D bird-view feature maps reshaped from the output of 3D backbone network for further feature abstraction. The detection header is composed of two sibling 1×1 convolutions with filter numbers of 256, which generates high-quality 3D proposals for the following graph construction. As for *Voxel-Point-Hybrid module*, we use MLPs of unit $(32+64+64, 64)$ for feature transformation, followed by two branches of units $(64, 1), (64, 3)$ for foreground classification and the center offset estimation. Also, we train a lightweight tiny PointNet-like block from scratch, of which two neighboring radii of each level are set as $(0.1m, 0.5m), (0.5m, 1.0m), (1.0m, 2.0m)$ respectively. The keypoints sampled for each level is set to 4,096, 1,024, 256 via FPS algorithm [25]. Finally, with regard to *boundary-aware graph neural network*, we stack three MLPs of units $(64+28+28, 60, 30, 120)$ with ReLU non-linearity for computing edges and updating nodes of local neighborhood graphs.

4.1.3 Training. Our BANet consumes regular voxels as input, so we first voxelize the raw point clouds with a quantization step of [0.05m, 0.05m, 0.1m]. Note that only objects in FOV are annotated for KITTI Dataset, we follow [10, 17, 39, 44, 46] to clip the range of point clouds into [0, 70.4]m, [-40, 40]m, and [-3, 1]m along the x, y, z axes, respectively. The resolution of final BEV feature map is 200 × 176. Hence, a total of 200 × 176 × 2 pre-defined anchors with same dimensions (width=1.6m, length=3.9m, height=1.56m) in statistics over the whole dataset for car category are evenly generated, with two possible orientations (0° or 90°) being considered. Furthermore, we follow the matching strategy of VoxelNet[46] to distinguish the negative and positive anchors with IoU thresholds 0.45 and 0.6 respectively.

The whole architecture of our BANet is optimized from scratch in an end-to-end fashion with SGD optimizer. We report the performance claimed in this paper by training the entire network for 50 epochs on a single GTX 1080 Ti GPU. We set batch size to 2, weight decay to 0.001. The learning rate is initialized with 0.01, which is decayed with a cosine annealing strategy adopted in SA-SSD [10]. During training, we consider frequently adopted data augmentations to facilitate our BANet's generalization ability, including global rotation around z-axis with the noise uniformly drawn from $[-\frac{\pi}{4}, \frac{\pi}{4}]$, global scaling with the scaling factor uniformly drawn from [0.95, 1.05], and global flipping along x-axis simultaneously. Also, we adopt a ground-truth augmentation strategy proposed by SECOND [39] to enrich the current training scene by seamlessly “pasting” a fraction of new ground-truth boxes and the associated points that fall in them.

4.1.4 Inference. We select high-confidence bounding boxes with a threshold 0.3. We use non-maximum suppression (NMS) with a rotated IoU threshold 0.1 to remove redundancy. Please refer to BANet's source code for more details since we will enclose herewith implementation details.

4.2 Comparison with State-of-the-Arts

4.2.1 Evaluation Metric. We follow the *KITTI Dataset* protocol using *Interpolated AP@S_N Metric*, which indicates the mean precision of N equally spaced recall levels:

$$AP = \frac{1}{N} \sum_{r \in S} P_{\text{interpolate}}(r), \quad (7)$$

where $S = \left[q_0, q_0 + \frac{q_1 - q_0}{N-1}, q_0 + \frac{2(q_1 - q_0)}{N-1}, \dots, q_1 \right]$ is a subset for N recall levels, of which the precision interpolated for each recall level r is represented by:

$$P_{\text{interpolate}}(r) = \max_{\tilde{r}: \tilde{r} \geq r} P(\tilde{r}). \quad (8)$$

As a common practice, we report average precision (AP) with a rotated IoU threshold 0.7 for *Car* in terms of assessing the quality of our proposed BANet. From 08.10.2019, KITTI benchmark adopts the *Interpolated AP@S₄₀ Metric* with 40 recall levels

$S_{40} = [1/40, 2/40, 3/40, \dots, 1]$ as suggested in [36] for more fair evaluation. We follow the conventions as previous works [4, 10, 32, 44] do. We evaluate on the *test* set by submitting to online *test* server of which 40 recall positions are considered. We evaluate on *val* set with 11 recall positions $S_{11} = [0, 0.1, 0.2, \dots, 1]$ to compare with existing state-of-the-arts unless otherwise noted.

Table 1: Performance comparison with state-of-the-arts on KITTI test server. We report the Average Precision(AP) with 40 recall positions on both BEV and 3D object detection leaderboard of *Car* category with a rotated IoU threshold 0.7. The top performance is indicated in bold. Please refer to http://www.cvlabs.net/kitti/eval_object?benchmark=3d for the purpose of online validation.

Method	AP _{3D} (%)			AP _{BEV} (%)		
	Easy	Mod.	Hard	Easy	Mod.	Hard
VoxelNet[46], CVPR18	77.82	64.17	57.51	87.95	78.39	71.29
SECOND[39], Sensors18	83.34	72.55	65.82	89.39	83.77	78.59
PointPillars[17], CVPR19	82.58	74.31	68.99	90.07	86.56	82.81
Point-GNN[35], CVPR20	88.33	79.47	72.29	93.11	89.17	83.90
3DSSD[40], CVPR20	88.36	79.57	74.55	92.66	89.02	85.86
SA-SSD[10], CVPR20	88.75	79.79	74.16	95.03	91.03	85.96
MV3D[2], CVPR17	74.97	63.63	54.00	86.62	78.93	69.80
ConfFuse[19], ECCV18	83.68	68.78	61.67	94.07	85.35	75.88
F-PointNet[23], CVPR18	82.19	69.79	60.59	91.17	84.67	74.77
AVOD-FPN[16], IROS18	83.07	71.76	65.73	90.99	84.82	79.62
PointRCNN[33], CVPR19	86.96	75.64	70.70	92.13	87.39	82.72
MMF[18], CVPR19	88.40	77.43	70.22	93.67	88.21	81.99
3D-CVF[43], ECCV20	89.20	80.05	73.11	93.53	89.56	82.45
3D IoU Loss[45], 3DV19	86.16	76.50	71.39	91.36	86.22	81.20
Part-A ² [34], TPAMI20	87.81	78.49	73.51	91.70	87.79	84.61
STD[41], ICCV19	87.95	79.71	75.09	94.74	89.19	86.42
PV-RCNN[32], CVPR20	90.25	81.43	76.82	94.98	90.65	86.14
Voxel R-CNN[4], AAAI21	90.90	81.62	77.06	94.85	88.83	86.13
BANet (ours),	89.28	81.61	76.58	95.23	91.32	86.48
Improvement (↑ %)	-1.62	-0.01	-0.48	+0.20	+0.29	+0.52

Table 2: Performance comparison with state-of-the-arts on *val* set. We report the Average Precision(AP) with 11 recall positions on 3D object detection leaderboard of *Car* category with a rotated IoU threshold 0.7. The top performance is indicated in bold.

Method	AP _{3D} (%)		
	Easy	Moderate	Hard
SECOND[39], Sensors18	87.43	76.48	69.10
PointPillars[17], CVPR19	-	77.98	-
PointRCNN[33], CVPR19	88.88	78.63	77.38
3DSSD[40], CVPR20	89.71	79.45	78.67
CIA-SSD[44], AAAI21	90.04	79.81	78.80
SA-SSD[10], CVPR20	90.15	79.91	78.78
MV3D[2], CVPR17	71.29	62.68	56.56
F-PointNet[23], CVPR18	83.76	70.92	63.65
ConfFuse[19], ECCV18	86.32	73.25	67.81
AVOD-FPN[16], IROS18	84.41	74.44	68.65
Fast Point R-CNN[3], ICCV19	89.12	79.00	77.48
STD[41], ICCV19	89.70	79.80	79.30
PV-RCNN[32], CVPR20	-	83.90	-
Voxel R-CNN[4], AAAI21	89.41	84.52	78.93
BANet (ours),	90.06	85.77	79.00

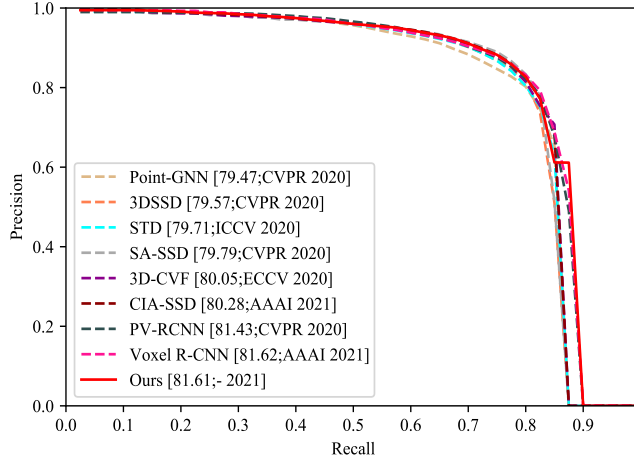


Figure 3: Precision × Recall curve of state-of-the-art methods on online KITTI 3D detection benchmark. We report average precision (AP) with a rotated IoU threshold 0.7 for *Moderate* difficulty of *Car* category.

Table 3: Effect of each feature component of region feature aggregation network.

$f^{(pixel)}$	$f^{(voxel)}$	$f^{(point)}$	AP_{3D} (%)			AP_{BEV} (%)		
			Easy	Mod.	Hard	Easy	Mod.	Hard
✓			90.04	79.78	78.91	90.64	89.12	80.49
✓			89.93	79.81	78.83	90.65	88.68	87.95
✓	✓		90.00	79.93	78.88	90.60	88.87	88.04
	✓		87.85	76.24	72.96	89.60	82.83	78.73
	✓	✓	88.36	76.96	74.10	89.87	83.62	79.09
	✓	✓	88.58	77.88	75.37	89.93	84.65	79.48
✓	✓		90.07	79.95	78.93	90.62	88.90	88.08
✓	✓		89.99	80.00	78.97	90.57	88.96	88.07
✓	✓	✓	90.06	85.77	79.00	90.63	88.86	88.10

Table 4: Ablation studies on the KITTI *val* set with T iterations of BANet.

Number of iterations	AP_{3D} (%)			AP_{BEV} (%)		
	Easy	Moderate	Hard	Easy	Moderate	Hard
T=0	79.18	75.61	74.86	79.18	75.61	74.86
T=1	85.68	80.16	77.84	88.72	88.13	87.76
T=2	89.24	83.11	78.91	90.15	88.63	87.99
T=3	90.07	85.74	78.99	90.60	88.85	88.09
T=4	90.28	85.79	79.11	90.71	88.97	88.17
T=5	90.02	79.87	78.85	90.65	88.83	88.11

4.2.2 KITTI Leaderboard. We compare the performance of our BANet on the KITTI *test* set with previous state-of-the-art methods by submitting predictions to the official online leaderboard [5, 6]. As shown in Table 1, Our BANet outperforms all its competitors with remarkable margins on KITTI BEV detection leaderboard and ranks 1st on *Car* category of *Moderate* difficulty, surpassing the second place, SA-SSD [10] by (0.2%, 0.29%, 0.52%) for *Easy*, *Moderate*, and *Hard* level respectively as of Apr. 17th, 2021. Note that our

backbone network at the first stage is built upon the architecture of SA-SSD while obtains an absolute gain by (0.53%, 1.82%, 2.42%) on 3D detection benchmark. To the best of our knowledge, little literature has achieved decent performance on 3D object detection via leveraging graph neural network until Point-GNN [35] is proposed. We surpass Point-GNN (0.95%, 2.14%, 4.29%) on 3D detection benchmark, (2.12%, 2.15%, 2.58%) on BEV detection benchmark while keep 3 × faster than Point-GNN (5.6 FPS vs. 1.5 FPS). Compared with the lastest state-of-the-art Voxel R-CNN [4], our BANet is slightly lower (-0.01%) but remains close on 3D detection benchmark while achieves (0.38%, 2.49%, 0.35%) improvement on BEV detection benchmark. Note that we outperform Voxel R-CNN by 2.49% on *Car* category of *Moderate* difficulty. Figure 3 further indicates better detection coverage of our BANet with different recall settings. Furthermore, we visualize some predictions from *test* set for qualitative comparison in Figure 4.

4.2.3 KITTI-val. In addition, as shown in Figure 2, we exploit *Interpolated AP@S₁₁ Metric* with a rotated IoU threshold 0.7 for further comparison with previous works on *val* set. Besides, by considering the results in Table 1, 2, we argue that such slightly inconsistent result between *val* set and *test* set plausibly can be reduced to the mismatched data distributions, as Part-A² [34] notes.

Overall, our BANet achieves decent performance on both *val* set and *test* set, which consistently demonstrates the effectiveness of our boundary-aware 3D detector.

4.3 Ablation Study

In this section, comprehensive ablation experiments are conducted to analyze the effectiveness of each component of our proposed BANet. Note that we report all results by *Interpolated AP@S₁₁ Metric* with a IoU threshold 0.7 unless otherwise noted. We train all our models on the *train* set and evaluate on the *val* set for the most important *Moderate* difficulty of *Car* category of KITTI Dataset [5, 6] [10, 32, 44].

4.3.1 Effect of region feature aggregation network. We judiciously investigate the effectiveness of each level feature component of ROI-wise representations in Eq. (3) by controlled experiments. As shown in the 3th, 4th, and 5th rows of Table 3, the performance of BANet deteriorates a lot when $f^{(pixel)}$ from BEV representation is absent. Nevertheless, it can not achieve state-of-the-art performance by itself. This is because the 8 × downsampling from 3D feature volumes progressively and the absence of 3D structure context when converting to BEV representation directly may degrade its localization accuracy. The aggregation from $f^{(pixel)}$, $f^{(voxel)}$, and $f^{(point)}$ significantly benefits the performance as shown in 6th to 9th rows. Note that each level feature component of x shows a supplementary effect more than a superposition. The 1st row indicates the performance of SA-SSD [10] reproduced from official source code. Considering SA-SSD is a single-stage method, we add a detect header on the top of SA-SSD for further comparison as shown 2nd row. As shown in the last row, the aggregation of all feature components contributes to the top performance with 85.77% AP on the *Moderate* difficulty of *Car* category.

4.3.2 Effect of boundary-aware 3D detector with T iterations. We propose boundary-aware 3D detector in Sec. 3.2 to model local

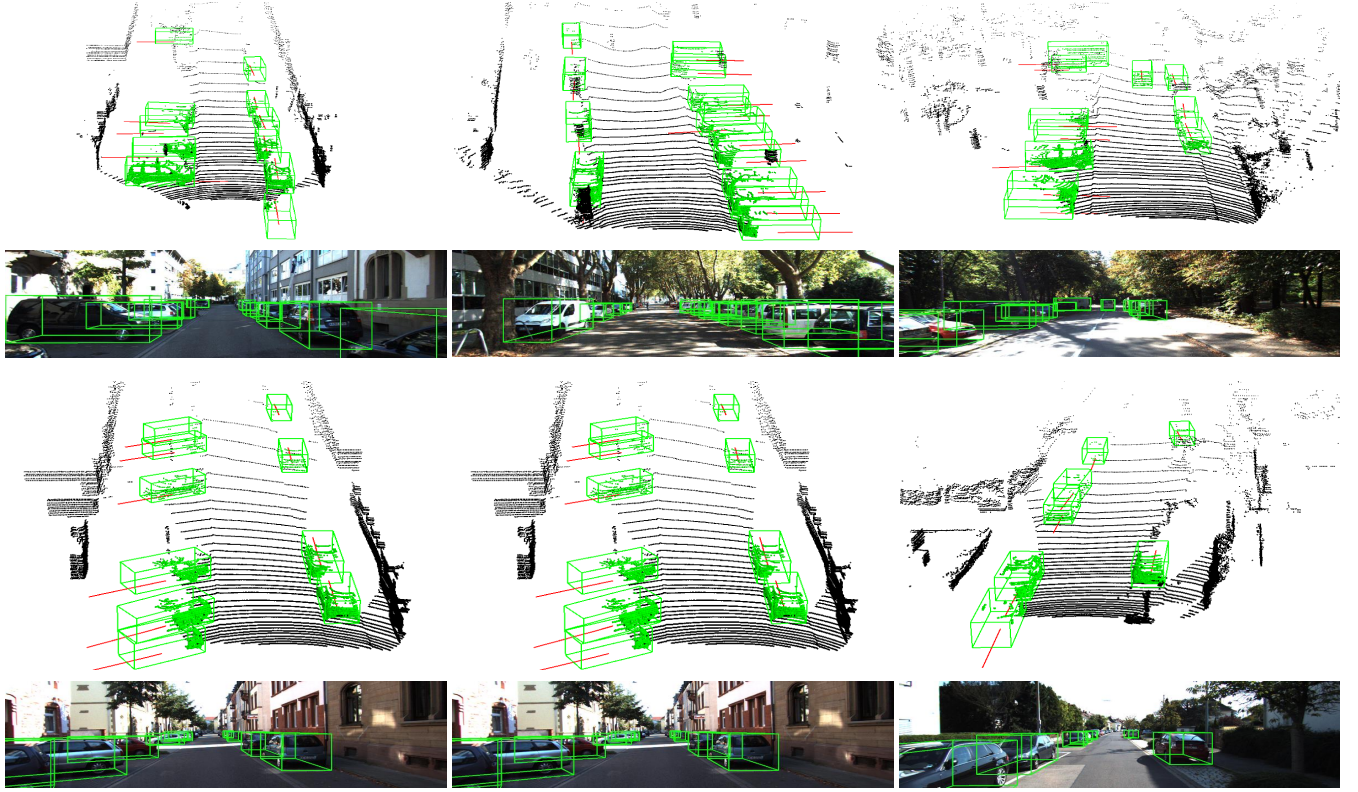


Figure 4: Qualitative results on KITTI *test* set using BANet. The predicted bounding boxes of Cars (in green) are drawn on both the point cloud (1st & 3rd) and the image (2nd & 4th). Best view in color.

boundary correlations of an object. Since graph neural network updates its nodes iteratively, the number of iterations is an important hyperparameter. As shown in Table 4, the 1st row shows the nodes' state initialized by \mathbf{x} can not achieve state-of-the-art performance without our information compensation mechanism. Note that the performance is significantly improved as the receptive field is expanding via graph edges with T iterations. We set T to 3 for online test server submission. Whereas, for *val* set, $T=4$ achieves the best performance. Particularly, when T is set to 5, the performance drops dramatically, which is likely due to the problem of gradient vanishing.

4.4 Runtime Analysis

The inference time is important for the deployment of downstream applications in the context of autonomous driving. Hence, we report a breakdown of runtime of our BANet for future optimization. Our BANet is implemented by Pytorch with Python language. We assess runtime on a single Intel(R) Core(TM) i7-6900K CPU and a single GTX 1080 Ti GPU. The average inference time (in millisecond) over *val* set (3769 samples) of BANet is 179 ms, which is 3 \times faster than Point-GNN [35] (5.6 FPS vs. 1.5 FPS): (i) Reading data before network forwarding takes 42.52ms (23.75%); (ii) 3D proposal generation in the first stage takes 63.56ms; (iii) Region feature aggregation network takes 5.64ms (3.15%); (iv) boundary-aware graph neural network takes 61.78ms (34.51%); and non-maximum suppression for filtering

redundancy takes 2.00ms (1.12%). In fact, as She et al. notes [35], factors affecting the runtime varies from software level (e.g., code optimization) to hardware level (e.g., GPU resources). Optimizing runtime is out of the scope of this paper. However, an analysis of inference time facilitates more follow-up works in this field.

5 CONCLUSIONS

In this paper, we present BANet framework, which provides an information compensation mechanism in the cases where proposals could not obtain enough information due to deviation. We model local boundary correlations of an object via local neighborhood graph, which explicitly facilitates a complete boundary for each individual proposal. Our BANet outperforms all previous state-of-the-art methods with remarkable margins on KITTI BEV detection leaderboard. The encouraging results on KITTI Dataset can set a new baseline for more follow-up literature and are poised to facilitate other downstream applications.

REFERENCES

- [1] Eduardo Arnold, Omar Y Al-Jarrah, Mehrdad Dianati, Saber Fallah, David Oxtoby, and Alex Mouzakitis. 2019. A survey on 3d object detection methods for autonomous driving applications. *IEEE Transactions on Intelligent Transportation Systems* (2019).
- [2] Xiaozhi Chen, Huimin Ma, Ji Wan, Bo Li, and Tian Xia. 2017. Multi-view 3d object detection network for autonomous driving. In *CVPR*.
- [3] Yilun Chen, Shu Liu, Xiaoyong Shen, and Jiaya Jia. 2019. Fast Point R-CNN. In *ICCV*.
- [4] Jiajun Deng, Shaoshuai Shi, Peiwei Li, Wengang Zhou, Yanyong Zhang, and Houqiang Li. 2020. Voxel R-CNN: Towards High Performance Voxel-based 3D

Object Detection. *CoRR* abs/2012.15712 (2020).

[5] Andreas Geiger, Philip Lenz, Christoph Stiller, and Raquel Urtasun. 2013. Vision meets robotics: The KITTI dataset. *CVPR* (2013).

[6] Andreas Geiger, Philip Lenz, and Raquel Urtasun. 2012. Are we ready for autonomous driving? the kitti vision benchmark suite. In *CVPR*.

[7] Ross Girshick. 2015. Fast R-CNN. In *ICCV*.

[8] Yulan Guo, Hanyun Wang, Qingyong Hu, Hao Liu, Li Liu, and Mohammed Bennamoun. 2019. Deep Learning for 3D Point Clouds: A Survey. *arXiv preprint arXiv:1912.12033* (2019).

[9] William L. Hamilton, Zhitao Ying, and Jure Leskovec. 2017. Inductive Representation Learning on Large Graphs. In *NeurIPS*.

[10] Chenhang He, Hui Zeng, Jianqiang Huang, Xian-Sheng Hua, and Lei Zhang. 2020. Structure Aware Single-stage 3D Object Detection from Point Cloud. In *CVPR*.

[11] Kaiming He, Georgia Gkioxari, Piotr Dollár, and Ross B. Girshick. 2017. Mask R-CNN. In *ICCV*.

[12] Kaiming He, Xiangyu Zhang, Shaoqing Ren, and Jian Sun. 2014. Spatial Pyramid Pooling in Deep Convolutional Networks for Visual Recognition. In *ECCV*.

[13] Max Jaderberg, Karen Simonyan, Andrew Zisserman, and Koray Kavukcuoglu. 2015. Spatial Transformer Networks. In *NeurIPS*.

[14] Licheng Jiao, Fan Zhang, Fang Liu, Shuyuan Yang, Lingling Li, Zhixi Feng, and Rong Qu. 2019. A Survey of Deep Learning-Based Object Detection. *IEEE Access* (2019).

[15] Thomas N. Kipf and Max Welling. 2017. Semi-Supervised Classification with Graph Convolutional Networks. In *ICLR*.

[16] Jason Ku, Melissa Mozifian, Jungwook Lee, Ali Harakeh, and Steven L Waslander. 2018. Joint 3d proposal generation and object detection from view aggregation. In *IROS*.

[17] Alex H Lang, Sourabh Vora, Holger Caesar, Lubing Zhou, Jiong Yang, and Oscar Beijbom. 2019. PointPillars: Fast encoders for object detection from point clouds. In *CVPR*.

[18] Ming Liang, Bin Yang, Yun Chen, Rui Hu, and Raquel Urtasun. 2019. Multi-Task Multi-Sensor Fusion for 3D Object Detection. In *CVPR*.

[19] Ming Liang, Bin Yang, Shenlong Wang, and Raquel Urtasun. 2018. Deep Continuous Fusion for Multi-sensor 3D Object Detection. In *ECCV*.

[20] Tsung-Yi Lin, Priya Goyal, Ross Girshick, Kaiming He, and Piotr Dollár. 2017. Focal loss for dense object detection. In *ICCV*.

[21] Wei Liu, Dragomir Anguelov, Dumitru Erhan, Christian Szegedy, Scott E. Reed, Cheng-Yang Fu, and Alexander C. Berg. 2016. SSD: Single Shot MultiBox Detector. In *ECCV*.

[22] Zhijian Liu, Haotian Tang, Yujun Lin, and Song Han. 2019. Point-Voxel CNN for Efficient 3D Deep Learning. In *NeurIPS*.

[23] Charles R Qi, Wei Liu, Chenxia Wu, Hao Su, and Leonidas J Guibas. 2018. Frustum pointnets for 3d object detection from rgbd data. In *CVPR*.

[24] Charles R Qi, Hao Su, Kaichun Mo, and Leonidas J Guibas. 2017. Pointnet: Deep learning on point sets for 3d classification and segmentation. In *CVPR*.

[25] Charles Ruizhongtai Qi, Li Yi, Hao Su, and Leonidas J Guibas. 2017. Pointnet++: Deep hierarchical feature learning on point sets in a metric space. In *NeurIPS*.

[26] Xiaojuan Qi, Renjie Liao, Jiaya Jia, Sanja Fidler, and Raquel Urtasun. 2017. 3D Graph Neural Networks for RGBD Semantic Segmentation. In *ICCV*.

[27] Zengyi Qin, Jingli Wang, and Yan Lu. 2020. Weakly Supervised 3D Object Detection from Point Clouds. In *ACM Multimedia*.

[28] Mohammad Muntasir Rahman, Yanhao Tan, Jian Xue, and Ke Lu. 2019. Recent advances in 3d object detection in the era of deep neural networks: A survey. *TIP* (2019).

[29] Joseph Redmon, Santosh Kumar Divvala, Ross B. Girshick, and Ali Farhadi. 2016. You Only Look Once: Unified, Real-Time Object Detection. In *CVPR*.

[30] Joseph Redmon and Ali Farhadi. 2016. YOLO9000: Better, Faster, Stronger. *CoRR* abs/1612.08242 (2016).

[31] Shaoqing Ren, Kaiming He, Ross B. Girshick, and Jian Sun. 2015. Faster R-CNN: Towards Real-Time Object Detection with Region Proposal Networks. In *NeurIPS*.

[32] Shaoshuai Shi, Chaoxu Guo, Li Jiang, Zhe Wang, Jianping Shi, Xiaogang Wang, and Hongsheng Li. 2020. PV-RCNN: Point-Voxel Feature Set Abstraction for 3D Object Detection. In *CVPR*.

[33] Shaoshuai Shi, Xiaogang Wang, and Hongsheng Li. 2019. Pointrcnn: 3d object proposal generation and detection from point cloud. In *CVPR*.

[34] Shaoshuai Shi, Zhe Wang, Jianping Shi, Xiaogang Wang, and Hongsheng Li. 2020. From Points to Parts: 3D Object Detection from Point Cloud with Part-aware and Part-aggregation Network. *TPAMI* (2020).

[35] Weijing Shi and Raghunathan (Raj) Rajkumar. 2020. Point-GNN: Graph Neural Network for 3D Object Detection in a Point Cloud. In *CVPR*.

[36] Andrea Simonelli, Samuel Rota Bulò, Lorenzo Porzi, Manuel Lopez-Antequera, and Peter Kortschieder. 2019. Disentangling Monocular 3D Object Detection. In *ICCV*.

[37] Lei Wang, Yuchun Huang, Yaolin Hou, Shenman Zhang, and Jie Shan. 2019. Graph Attention Convolution for Point Cloud Semantic Segmentation. In *CVPR*.

[38] Yue Wang, Yongbin Sun, Ziwei Liu, Sanjay E Sarma, Michael M Bronstein, and Justin M Solomon. 2019. Dynamic graph cnn for learning on point clouds. *TOG* (2019).

[39] Yan Yan, Yuxing Mao, and Bo Li. 2018. Second: Sparsely embedded convolutional detection. In *Sensors*.

[40] Zetong Yang, Yanan Sun, Shu Liu, and Jiaya Jia. 2020. 3DSSD: Point-based 3D Single Stage Object Detector. *CVPR* (2020).

[41] Zetong Yang, Yanan Sun, Shu Liu, Xiaoyong Shen, and Jiaya Jia. 2019. Std: Sparse-to-dense 3d object detector for point cloud. In *CVPR*.

[42] Maosheng Ye, Shuangjie Xu, and Tongyi Cao. 2020. HVNet: Hybrid Voxel Network for LiDAR Based 3D Object Detection. *CoRR* abs/2003.00186 (2020).

[43] Jin Hyeok Yoo, Yechol Kim, Ji Song Kim, and Jun Won Choi. 2020. 3D-CVF: Generating Joint Camera and LiDAR Features Using Cross-View Spatial Feature Fusion for 3D Object Detection. *ECCV*.

[44] Wu Zheng, Weiliang Tang, Sijin Chen, Li Jiang, and Chi-Wing Fu. 2020. CIA-SSD: Confident IoU-Aware Single-Stage Object Detector From Point Cloud. *AAAI* (2020).

[45] Dingfu Zhou, Jin Fang, Xibin Song, Chenye Guan, Junbo Yin, Yuchao Dai, and Ruigang Yang. 2019. IoU Loss for 2D/3D Object Detection. In *3DV*.

[46] Yin Zhou and Oncel Tuzel. 2018. Voxelnet: End-to-end learning for point cloud based 3d object detection. In *CVPR*.

[47] Zhengxia Zou, Zhenwei Shi, Yuhong Guo, and Jieping Ye. 2019. Object Detection in 20 Years: A Survey. *arXiv preprint arXiv:1905.05055* (2019).